Journal of Materials Chemistry A

Accepted Manuscript

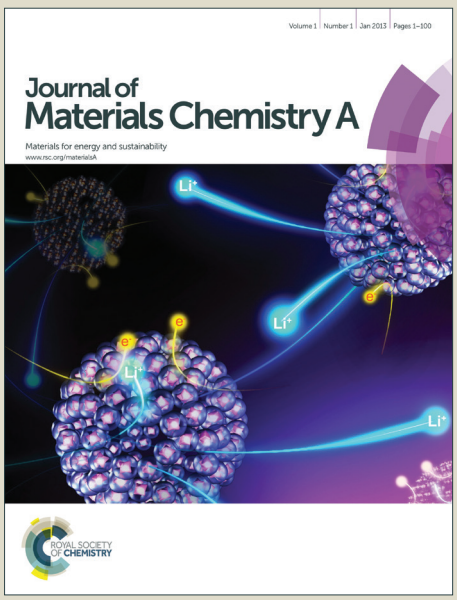

ROYAL SOCIETY OF CHEMISTRY

www.rsc.org/materialsA

High temperature structural stability, electrical properties and chemical reactivity of $NdBaCo_{2-x}Mn_xO_{5+\delta}$ ($0 \leq x \leq 2$) for use as cathode in Solid Oxide Fuel Cells

Thibault Broux[1], Mona Bahout[1*], James M. Hanlon[1], Olivier Hernandez[1], Serge Paofai[1], Andrey Berenov[2] and Stephen J. Skinner[2*]

[1]Institut des Sciences Chimiques de Rennes, Equipe « Chimie du Solide et Matériaux », UMR CNRS 6226, Université de Rennes 1, 263 Avenue du Général Leclerc, 35042 Rennes, France

[2] Department of Materials, Imperial College London, Exhibition Road, London SW7 2AZ, United Kingdom

ABSTRACT. The effects of Mn substitution for Co on the crystal chemistry, oxygen content thermal expansion and electrical conductivity of the $NdBaCo_{2-x}Mn_xO_{5+\delta}$ perovskites ($0 \leq x \leq 2$) has been investigated. The $NdBaCo_{2-x}Mn_xO_{5+\delta}$ samples exhibit structural change with increasing Mn content from orthorhombic ($x = 0$) to tetragonal ($0.5 \leq x \leq 1$) then cubic ($1.5 \leq x \leq 2.0$) symmetry. All the samples lose oxygen when heated in air at $T > 400$ °C although the degree of oxygen loss and kinetics of oxygen exchange between the gas phase and oxide decrease with increasing Mn content. The thermal expansion coefficients evaluated from *ex situ* XRD and electrical resistivity decrease with increasing Mn substitution and the values of the $x = 1.5$ and 2.0 compositions match those of the $Ce_{0.8}Gd_{0.2}O_{1.95}$ (GDC) and $La_{0.8}Sr_{0.2}Ga_{0.8}Mg_{0.2}O_{2.8}$ (LSGM) electrolytes. With electrical conductivity of > 100 S cm^{-1} at 800 °C and good chemical stability with GDC and LSGM, the Mn-substituted perovskites are promising cathode materials for SOFC.

Introduction

Solid oxide fuel cells (SOFC) offer two important advantages in comparison to proton exchange membrane fuel cells (PEMFCs) in that they operate with inexpensive non-platinum catalysts and can directly use hydrocarbon fuels without requiring external fuel reforming due to their higher operating

temperatures (above 500 °C). However, SOFC technology is confronted with slow oxygen reduction kinetics with conventional cathode materials at the intermediate operating temperatures of 500 - 800 °C. For example, the $La_{1-x}Sr_xMnO_{3-\delta}$ standard cathode typically operates at around 1000 °C [1] but shows poor oxide-ion conductivity and inadequate catalytic activity at 500 - 800 °C because of the stability of Mn^{4+} ions at these intermediate temperatures and the difficulty of creating oxygen vacancies in the lattice [2-3]. In this regard, the cobalt-based perovskite cathodes such as $La_{1-x}Sr_xCoO_{3-\delta}$ are appealing as they show good mixed ionic and electronic conductivity (MIEC) at 700 - 800 °C [2-5]. However, the use of $La_{1-x}Sr_xCoO_{3-\delta}$ (LSC) in practical SOFCs is an issue due to their much higher thermal expansion coefficients (TEC) compared to those of standard electrolyte materials [3, 6]. Despite optimization by various cation substitutions at both the *A* and *B* sites [2, 4, 7], the perovskites still fail to operate at the low temperatures of ~ 500 °C required for the commercialization of fuel cell technology. Clearly the development of alternative cathode materials demonstrating high oxygen diffusivity, adequate catalytic activity and acceptable *TEC* at these low temperatures is critical for the realization of an intermediate temperature SOFC technology.

Recently, promising MIEC properties in the layered double perovskites $LnBaCo_2O_{5+\delta}$ (*Ln* = Y and lanthanide) have stimulated exploration of their application as cathodes in SOFCs [8-13]. The structure of $LnBaCo_2O_{5+\delta}$ consists in *Ln*-O and Ba-O layers alternately stacked along the *c*-axis with oxygen vacancies in the *Ln*O layer. This structure is similar to that of $YBaCuFeO_5$ [14-15], the first compound reported with this structure-type. The oxygen content in $LnBaCo_2O_{5+\delta}$ can vary significantly ($0 \leq \delta \leq 1$) depending on the nature of the *Ln* cation, synthesis atmosphere and heat treatments. The δ value affects the crystal structure which can be either tetragonal *P*4/*mmm* ($a_p \times a_p \times 2a_p$), orthorhombic *Pmmm* ($a_p \times 2a_p \times 2a_p$ or $a_p \times a_p \times 2a_p$) or orthorhombic *Pmmb* ($a_p \times 2a_p \times 2a_p$) where *p* refers to the cubic perovskite cell parameter (*ca.* 3.9 Å) [16-18]. The doubling in *c* is due to ordering of *Ln* and Ba into layers perpendicular to *z*. The doubling in *b* has been suggested to arise from oxygen vacancy ordering in empty chains running along the *a*-axis at a value of $\delta \sim 0.5$ [19-20]. High temperature X-ray diffraction data

obtained in air revealed an orthorhombic to tetragonal transition associated with oxygen vacancy order-disorder at $T \sim 350$ °C [21]. As with the LSC perovskites, thermal compatibility is a critical issue for cobalt-rich cathodes, due to the higher TEC of these materials. Generally, the high TEC of cobalt-based cathodes is mainly related to oxygen loss along with the reduction of Co^{4+} to Co^{3+} that is accompanied by a spin transition of the Co^{3+} ion from a low spin ($t_{2g}^6 e_g^0$) to intermediate ($t_{2g}^5 e_g^1$) or high spin ($t_{2g}^4 e_g^2$) [22-24]. The substitution of various transition metals M = Fe, Ni and Cu for Co has been investigated with the aim of lowering the TEC and were shown to affect the crystal structure, oxygen content and oxygen diffusion properties [25-28]. In contrast to M = Ni and Cu where a limited substitution range is possible in $NdBaCo_{2-x}M_xO_{5+\delta}$ with $x \leq 0.6$ and 1.1 for Ni and Cu respectively [25, 28-29], complete substitution of Co is possible ($0 \leq x \leq 2$) when using Fe or Mn [30-37]. The particular interest in Mn substitution in the $NdBaCo_{2-x}M_xO_{5+\delta}$ system relates to the rich variety of chemistry observed in $NdBaCo_2O_{5+\delta}$ and $NdBaMn_2O_{5+\delta}$. In the present study, we explore the structure, electrical properties, thermal behaviour, oxygen diffusion and chemical reactivity with the electrolytes of the $NdBaCo_{2-x}Mn_xO_{5+\delta}$ compositions with x = 0, 0.5, 1, 1.5 and 2. Our aim is to identify broad trends for more thorough study in view of applications for SOFCs. We chose Nd as the lanthanide since previous studies on the high temperature properties of $LnBaCo_2O_{5+\delta}$ (Ln = La, Nd, Sm, Gd and Y) showed that the Nd sample exhibits good cathode performance, comparable to that of $La_{0.5}Ba_{0.5}Co_{0.5}O_{3-\delta}$ but still with high TEC (22.4×10^{-6} K^{-1}) in the temperature range of 80 - 900 °C [29]. Mn substitution for Co should also lower the TEC to reasonable values while retaining good electrical and electrochemical performance for the cathode material.

The structure and physical properties of the Co and Mn perovskites (*i.e.* x = 0.0 and 2.0 members) have been the subject of a number of studies [13, 18, 21, 33, 35-36, 38-41]. The $NdBaCoMnO_5$ (x = 1.0, δ = 0) composition has been obtained previously using a mass-flow controlled reducing reaction. Heating at 800 °C in air for 6 h produced the oxidized compound $NdBaMnCoO_6$ (δ = 1) [37]. Conversely, the x = 0.5 and x = 1.5 members have not been reported until the current work.

Experimental

Polycrystalline 5g samples of $NdBaCo_{2-x}Mn_xO_{5+\delta}$ (x = 0, 0.5, 1.0 and 1.5) perovskite oxides were synthesized by a combined EDTA-citrate complexing sol-gel process. Stoichiometric amounts of $Nd(NO_3)_3 \cdot 6H_2O$ (Sigma Aldrich, 99.9% purity), $Ba(NO_3)_2$ (Sigma Aldrich, ≥ 99% purity), $Co(NO_3)_2 \cdot 6H_2O$ (Sigma Aldrich, ≥ 99% purity) and $Mn(NO_3)_2 \cdot 4H_2O$ (Sigma Aldrich, ≥ 99% purity) were dissolved in distilled water. Two equivalents of citric acid per mole of metal cation and 1 equivalent of EDTA (Sigma Aldrich, ≥ 98.5% purity) per mole of metal were added. To ensure a complete dissolution of EDTA, ammonium hydroxide (Carlo Ebra, analysis grade) was added. The acidic solution (pH ~ 4) was then heated up to 150 °C with constant stirring. A pink gel formed then transformed to a spongy resin that was heated in a muffle furnace at 550 °C overnight to decompose most of the organic components. The resulting brown powder was ground then pressed into pellets (2 mm thickness, 13 mm diameter) that were annealed at 1200 °C for 6 h in static air for the pure cobalt compound (x = 0) and under 1 atm of flowing argon for the manganese containing samples (x = 0.5, 1.0, 1.5 and 2). Commercial electrolyte powders, $Ce_{0.8}Gd_{0.2}O_{1.95}$ (GDC), Fuel Cell Materials and $La_{0.8}Sr_{0.2}Ga_{0.8}Mg_{0.2}O_{3-\delta}$, (LSGM), Praxair Inc, USA, electrolytes were pressed and sintered at temperatures up to 1500 ^oC to form dense bodies to deposit the cathodes on. Phase purity of all materials was assessed by powder X-ray diffraction (XRD) over the range $10 \leq 2\theta/° \leq 120$, $\Delta 2\theta = 0.02°$ using a Bruker AXS D8 Advance diffractometer in Bragg-Brentano geometry equipped with Ge primary monochromator (Cu-$K\alpha_1$ radiation) and a Lynxeye detector. Rietveld refinements were performed using the FullProf software [42]. A Pseudo-Voigt peak-shape was used as the profile function.

Thermogravimetric analysis (TGA) was performed with a Netzsch (STA 449F3) thermal analysis system. The TGA experiments were carried out in 1 atm of air or 5%H_2-95%N_2 (40 mL min^{-1}) using samples weighing ~ 100 mg loaded in alumina crucibles. The temperature profile in air consists of heating to 800 °C at 2 °C min^{-1} followed by 6 h isotherm at 800 °C (to equilibrate the oxygen content at

the highest temperature at which the electrical conductivity has been measured) before cooling at 2 °C min^{-1} to *RT*.

The average oxidation state of the mean transition metal cation $(Co_{2-x}Mn_x)^{3+/4+}$ and the oxygen content of the as-prepared samples were determined by iodometric titration against a standardized sodium thiosulfate solution (~ 0.05 M). A powder sample (~ 300 mg) of $NdBaCo_{2-x}Mn_xO_{5+\delta}$ was introduced in a closed argon-flushed glass container and covered by a large excess of KI (~ 2 g). Approximately 20 mL of hydrochloric acid twice diluted was added to the warm mixture that was stirred under an argon flow. When dissolution was complete, the iodine formed was titrated under argon flow with $Na_2S_2O_3$ solution and the calculated oxygen stoichiometry was based on the amount of I_2 formed. Electrical conductivity of dense bars (relative densities > 90% measured by a liquid displacement technique) sintered at 1250 °C for 12 h in air (x = 0.0) or argon (x = 0.5, 1.0, 1.5 and 2.0) was measured in air with a dc four-probe method with Pt contacts on bars with approximate dimensions of 3 mm × 3 mm × 12 mm. Measurements were performed at 100 °C intervals on cooling from 800 to 200 °C and subsequent heating. A constant value of current (adjusted between 1 and 90 mA depending on the voltage measured) was applied. The samples were held for between 3 and 6 hours at each temperature to allow for stabilization of the voltage response.

Chemical stability with GDC and LSGM electrolytes was evaluated by heating a mixture of $NdBaCo_{2-x}Mn_xO_{5+\delta}$ and LSGM/GDC powders (1:1 molar ratio) at 800 °C for 36 h in air. *Ex-situ* XRD patterns were then collected to reveal any composition change after this heat treatment.

Results and discussion

1. *Structural and chemical analysis*

XRD data recorded at room temperature (*RT*) show that single-phase $NdBaCo_{2-x}Mn_xO_{5+\delta}$ with x = 0, 0.5, 1.0, 1.5 were obtained after annealing at 1200 °C for 12 h. For x = 2.0, the XRD pattern exhibits small extra peaks (labeled * in Figure 1) identified as corresponding to a hexagonal $BaMnO_{3-\delta}$

perovskite impurity [43-44] whose fraction is negligible (< 2 wt %). Therefore, the contribution of Mn from $BaMnO_3$ to the oxidation state of the $x = 0.2$ phase is insignificant.

The XRD patterns of $x = 0$, 0.5 and 1.0 samples are consistent with the ordering of Nd^{3+} and Ba^{2+} in alternate layers. For $x = 0$, the pattern was indexed on an orthorhombic unit cell with the space group *Pmmm* while the patterns for $x = 0.5$ and 1.0 were indexed on a tetragonal unit cell with the space group *P*4/*mmm*.

No peaks consistent with *A*-site ordering were observed for the $x = 1.5$ and 2.0 samples whose patterns were indexed on a cubic unit cell with the space group *Pm*-3*m*. Table 1 lists the values of cell parameters and oxygen content determined from iodometric titration.

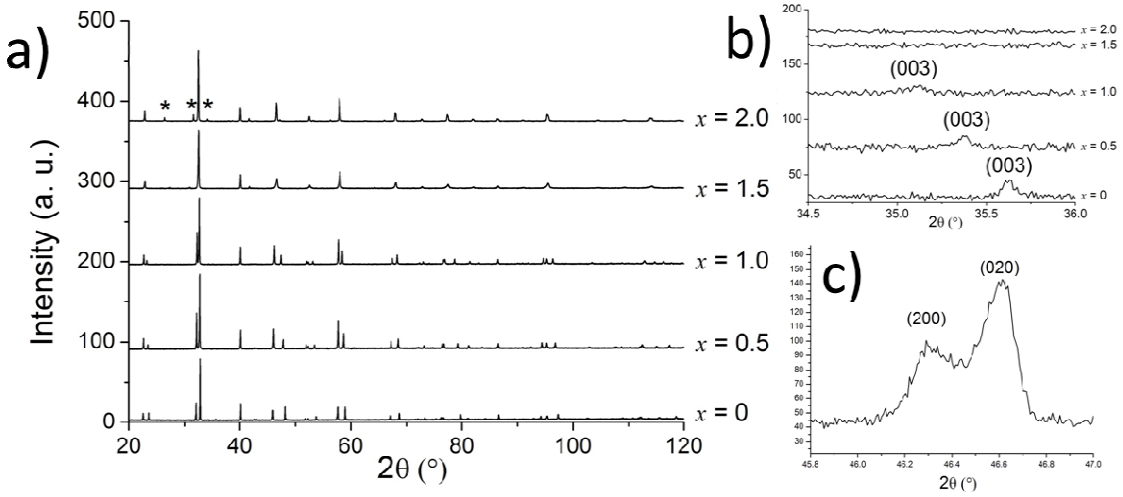

Figure 1. a) XRD patterns of $NdBaCo_{2-x}Mn_xO_{5+\delta}$ at room temperature after 12 h annealing at 1200 °C in air ($x = 0$) or Ar ($x = 0.5$, 1.0, 1.5 and 2.0) and subsequent cooling at 3 °C min^{-1}. The reflections labeled * in $x = 2.0$ belong to a hexagonal $BaMnO_{3-\delta}$ impurity phase (<2 wt %), b) (00*l*) peak in $x = 0$, 0.5 and 1.0 reflect the ordering of Nd^{3+} and Ba^{2+}, c) (200) and (020) reflections are consistent with orthorhombic symmetry in $x = 0$.

The $NdBaCo_2O_{5+\delta}$ ($x = 0$) material crystallizes in tetragonal *P*4/*mmm* ($a_p \times a_p \times 2a_p$) or orthorhombic *Pmmm* ($a_p \times a_p \times 2a_p$ or $a_p \times 2a_p \times 2a_p$) symmetry where *p* refers to the parent perovskite. The structure at *RT* is strongly correlated to the oxygen content which depends on synthesis atmosphere and cooling

rate [45]. An earlier study suggested $NdBaCo_2O_{5+\delta}$ with $\delta \sim 0.69$ to be orthorhombic [20] whereas tetragonal structures were reported for $\delta \sim 0.85$ [25] and $\delta \sim 0.70$ [46]. As shown in Table 1, our $x = 0$ sample has lower oxygen content, $\delta \sim 0.55(3)$ compared to those reported in [25, 46] indicating that our cooling rate (3 °C min^{-1}) did not allow maximization of the δ value to give a tetragonal structure. The XRD pattern can be indexed on an $a_p \times a_p \times 2a_p$ pseudo-tetragonal unit cell within the resolution of our data and technique. Indeed, an orthorhombic distortion is clearly evidenced by the 200/020 doublet at d ~1.96 Å (Figure 1 c). The orthorhombic *Pmmm* ($a_p \times 2a_p \times 2a_p$) unit cell is usually reported for $LnBaCo_2O_{5+\delta}$ at $\delta \sim 0.5$ [46] and involves ordering of the oxygen vacancies into channels perpendicular to *y*. At lower oxygen content, $\delta \sim 0.44$ [47] and 0.38 [20], a *Pmmm* ($a_p \times a_p \times 2a_p$) structure with disordered oxygen vacancies is observed. The difference between *a* and *b* unit cell parameters in our $x = 0$ material might be due to weak ordering of the oxygen vacancies within the *ab* plane [20] which could not be detected from our diffraction data due to the low X-ray scattering factor of the oxygen atoms compared to those of the heavier Ba and Nd atoms and the low statistics of our diffraction data compared to that obtained from a synchrotron source.

The oxidized and reduced $NdBaCoMnO_{5+\delta}$ materials, respectively with $\delta = 0$ and $\delta = 1$, have been prepared previously *via* a solid-state route with mass-flow control of reducing reaction atmosphere. The structures at *RT* from neutron powder diffraction were found to be tetragonal and show full order of the *A*-site cations and no order of the *B*-site cations [37]. Here, a sol-gel synthesis route with an argon annealing atmosphere allows a single tetragonal phase to be obtained. The oxygen content $\delta \sim 0.67(3)$ and lattice parameters (Table 1) are between those reported by Snedden *et al*. for the oxidized (a = 3.89310(2), c = 7.69753(7) Å) and reduced (a = 3.94071(2), c = 7.69532(6) Å) phases [37].

The $x = 0.5$ and 1.5 compositions have not been reported so far. The former shows full order of the *A*-site cations, similar to the $x = 0$ and 1 compositions and its XRD pattern was indexed on *P4/mmm* symmetry while the $x = 1.5$ and $x = 2.0$ samples do not show the peaks ($2\theta \sim 11.1°$ and $2\theta \sim 35.3°$)

characteristic of *A*-site ordering (Figure 1). These materials can be described as cubic, having a lattice parameter $a \sim 3.89$ Å (Table 1). Therefore, ordering of the lanthanide and barium is not only promoted by the difference between the ionic radii of the Ba and Nd cations but also depends on the *B*-site cation and oxygen content.

The system $NdBaCo_{2-x}Mn_xO_{5+\delta}$ exhibits the same crystal chemistry as $NdBaCo_{2-x}Fe_xO_{5+\delta}$ [30]. Indeed, the XRD patterns of the latter series could be indexed on the *P*4/*mmm* tetragonal space group for $0 \leq x \leq 1.4$ and *Pm*-3*m* cubic space group for $1.5 \leq x \leq 2.0$ [30].

The synthesis of the pure manganites $LnBaMn_2O_{5+\delta}$ (*Ln* = Y, La, Pr, Nd) was reported to be difficult. For example, to obtain a single $YBaMn_2O_{5+\delta}$ material, long reaction times in controlled atmosphere (argon containing less than 1 ppm of O_2) are required [48]. In the $La_{1-y}Ba_yMnO_3$ system, the synthesis of barium-rich compositions ($y > 0.4$) usually leads to the formation of hexagonal $BaMnO_{3-\delta}$ impurities [43-44].

A pure polycrystalline $Nd_{0.5}Ba_{0.5}MnO_{3-\delta}$ phase has not been reported so far; only single crystals were grown by the floating-zone method [49]. To prevent the formation of the $BaMnO_{3-\delta}$ secondary phase in the $x = 2$ sample, the barium content was reduced. A molar ratio of Ba/Nd = 0.9 decreased the amount of the $BaMnO_{3-\delta}$ and a ratio of Ba/Nd = 0.8 led to single $NdBa_{0.8}Mn_2O_{5+\delta}$ cubic phase with 20% vacancies at the *A*-site (Figure 2). Such deficiency is not detrimental for SOFC applications. Indeed, Shengli *et al.* reported that the electrochemical performance of $PrBaCo_2O_{5+\delta}$ was improved by introducing barium deficiency at the *A*-site [50]. The lattice parameters and oxygen content of the different samples prepared are listed in Table 1.

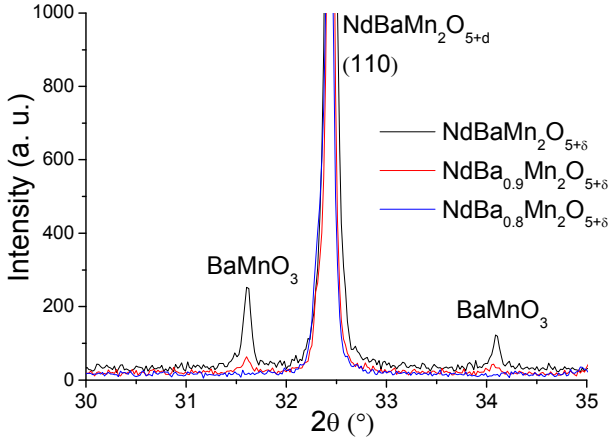

Figure 2. Part of the XRD patterns of $NdBa_{1-y}Mn_2O_{5+\delta}$ (y = 0, 0.1, 0.2) annealed in argon at 1200 °C for 6 h showing the decrease of the $BaMnO_3$ impurity as *A*-site deficiency increases.

Table 1. Space group and lattice parameters of as-prepared $NdBaCo_{2-x}Mn_xO_{5+\delta}$; x = 0 was annealed in air while x = 0.5, 1.0, 1.5 and 2.0 were annealed in argon. The oxygen content was determined from iodometric titration (accuracy of ± 0.03).

Manganese content (x)	Space group	a (Å)	b (Å)	c (Å)	Oxygen content (δ)	(Co,Mn) oxidation state
0	*Pmmm*	3.94560(3)	3.95208(3)	7.57080(5)	5.55(3)	95% M^{3+} 5% M^{4+}
0.5	*P4/mmm*	3.94016(4)	-	7.62584(6)	5.56(3)	94% M^{3+} 6% M^{4+}
1.0	*P4/mmm*	3.92757(3)	-	7.67617(6)	5.67(3)	83% M^{3+} 17% M^{4+}
1.5	*Pm-3m*	3.89518(5)	-	-	5.89(3)	61% M^{3+} 39% M^{4+}
2.0	*Pm-3m*	3.89675(3)	-	-	5.97(3)	53% M^{3+} 47% M^{4+}

Figure **3** shows the evolution of unit-cell parameters and *c*/*a* ratio for $NdBaCo_{2-x}Mn_xO_{5+\delta}$ as a function of *x*. We can clearly distinguish two different regions:

i. $0 \leq x \leq 1.0$; the system exhibits an *A*-site ordered structure providing an orthorhombic ($x = 0$) or tetragonal ($x = 0.5, 1.0$) symmetry.

ii. $1.5 \leq x \leq 2.0$; the system has evolved to a cubic symmetry (S.G. *Pm*-3*m*) with a lattice parameter $a \sim 3.9$ Å and the Nd and Ba cations are disordered at the *A*-site.

Table 1 and Figure 3 indicate that with increasing Mn-content from $x = 0$ to $x = 1.0$, the ordering of the *A*-site cations remains, providing a tetragonal structure, albeit with a reduced level of distortion, indicated by the increase in the *c*/*a* ratio. The lower distortion is caused by an expansion along *c* coupled with a contraction along *a*. The *B*-site cations move towards the plane of the equatorial oxygen anions upon increased Mn-content, given that manganese is more electropositive than cobalt ($\chi_{Co} = 1.88$, $\chi_{Mn} = 1.55$, in the Pauling scale [51]). The decrease in the *a* lattice parameter can also be explained by the smaller ionic radius of Mn^{4+} (0.53 Å) with respect to Co^{3+} (0.54 Å) [52]. Since *A*-site ordering in the layered perovskites is promoted by the oxygen vacancies in the *Ln*O layer, the transition towards an A-site disordered structure at $x = 1.5$ is likely induced by the increase of oxygen-content (Table 1). Coordination number depends on the relative size of the ions. Nd^{3+} cation (ionic radius ~ 1.27 Å) has a preference for smaller coordination number than Ba^{2+} cation (ionic radius ~ 1.61 Å). In the Co-rich phases $NdBaCo_{2-x}Mn_xO_{5+\delta}$ ($x \leq 1$) where a large amount of oxygen vacancies exists, they will preferentially form around Nd^{3+} rather than Ba^{2+}. Such situation will favour segregation of Nd^{3+} and Ba^{2+} in different layers (i.e. *A*-site ordering).

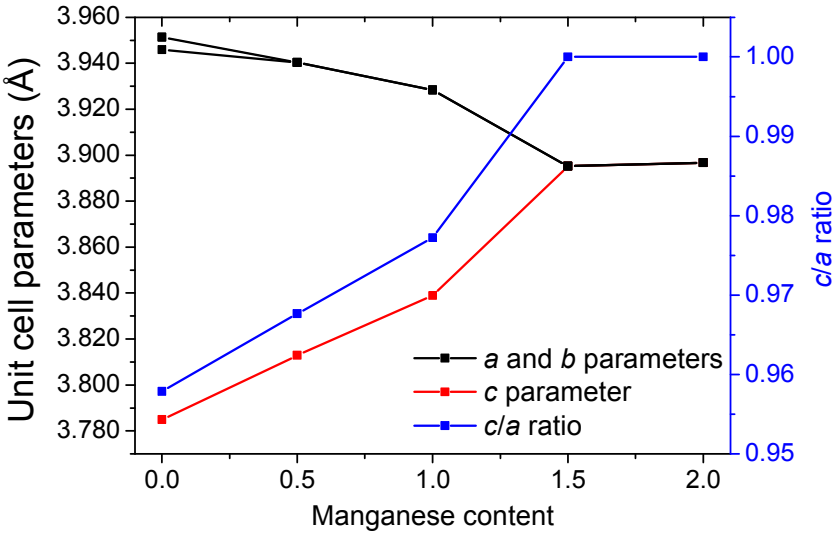

Figure 3. Variation of the unit-cell parameters and the *c*/*a* ratio for $NdBaCo_{2-x}Mn_xO_{5+\delta}$ as a function of manganese content (*x*) at *RT*. The *c* parameter of the layered perovskites (*x* = 0, 0.5 and 1.0) is divided by two for comparison with that of the cubic phases (*x* = 1.5 and 2.0). Error bars are smaller than symbol size.

2. Thermogravimetric analysis (TGA)

TGA on the $NdBaCo_{2-x}Mn_xO_{5+\delta}$ samples has been carried out in air from room temperature up to 800 °C on heating at 2 °C min^{-1}. At 800 °C, the samples were held isothermally for 6 h before cooling at 2 °C min^{-1} to *RT*. The evolution of the oxygen composition as a function of temperature determined from the weight change is illustrated in Figure 4 assuming the initial oxygen content obtained from iodometric titration. Once again, we can clearly distinguish two different behaviors:

i. $0 \leq x \leq 1.0$; the *A*-site ordered compounds gain oxygen on heating with a maximum rate at 300 - 350 °C then display a rapid weight loss at $T > 400$ - 450 °C attributed to the loss of weakly bonded lattice oxygen which correspond to the reduction of Co^{4+}/Mn^{4+} to Co^{3+}/Mn^{3+}. The degree of oxygen loss decreases with increasing Mn content. On isothermal heating at 800 °C, the δ value does not vary indicating that the equilibrium state has been reached under dynamic heating. On subsequent cooling, the samples uptake oxygen down to $T\sim$ 300 °C while on further cooling the oxygen content remains constant. The δ values at *RT* after the heating/cooling cycle are larger than those in the as-prepared

materials (Table 2) indicating that the cooling rate of 2 °C min^{-1} used for the synthesis did not allow equilibration of the oxygen stoichiometry. The amount of oxygen loss on heating above 350-400 °C as well as that of oxygen uptake on cooling from 800 °C to *RT* decreases with increasing Mn content (Table 2). This is related to the stability of the Mn^{4+} oxidation state at elevated temperatures (T < 800 °C) which results in little or no oxygen vacancies as observed in the $La_{1-x}Sr_xMnO_3$ perovskite cathode.

ii. For $1.5 \leq x \leq 2.0$; there is no oxygen uptake on heating in air although the samples have been preapared in an argon atmosphere. The x = 1.5 sample loses oxygen on heating at T > 500 °C and the mass continues to decrease during the 6 h of isothermal dwell at 800 °C without reaching equilibrium. This behaviour suggests that the oxygen exchange process between the solid oxide and oxygen in the gaseous phase is slow, likely limited by slow surface exchange kinetics as confirmed by insignificant mass change on cooling (Table 2). In contrast to the other compositions, the x = 2.0 sample does not exhibit significant mass change in air throughout the heating/cooling cycle and intermediate isotherm for 6 h at 800 °C. This behaviour can be explained by the higher stability of Mn^{4+} at elevated temperatures in comparison to Co^{4+} and the stronger Mn-O bonds with respect to Co-O bonds.

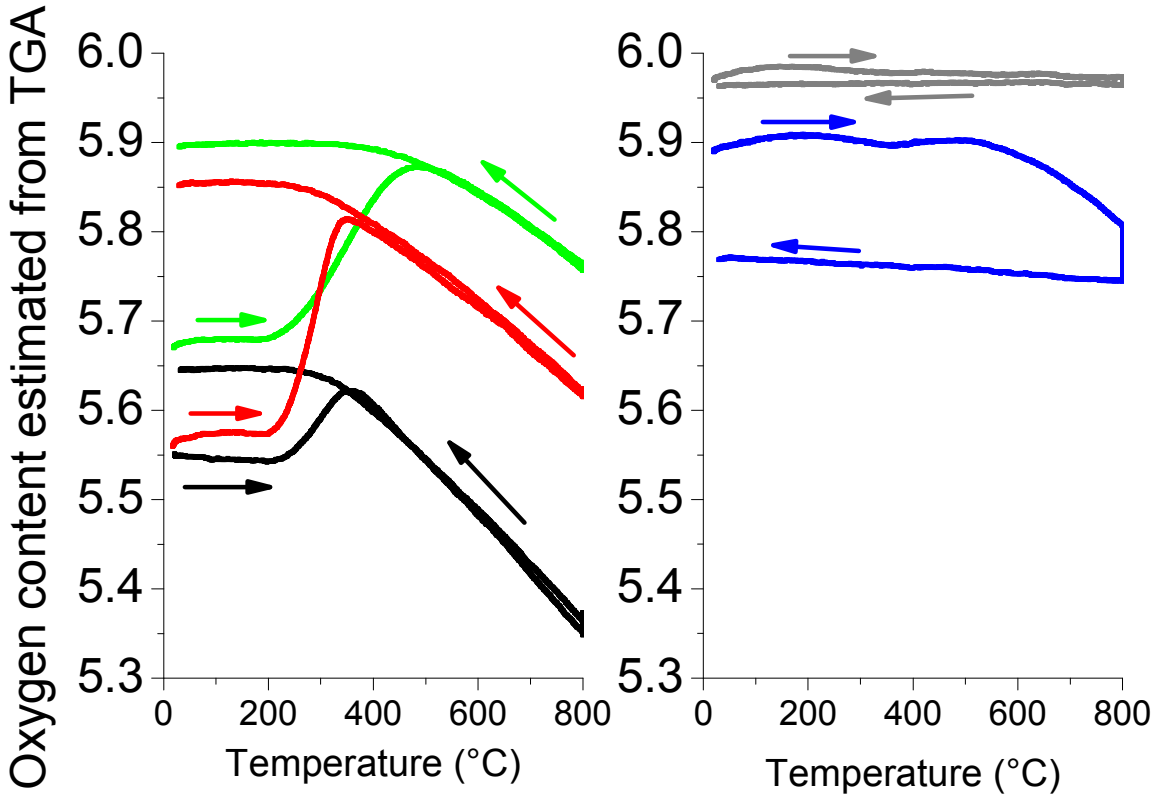

Figure 4. Oxygen content of $NdBaCo_{2-x}Mn_xO_{5+\delta}$ from TGA. The samples were heated in air at 2 °C min^{-1} and held isothermally for 6 h at 800 °C before cooling at 2 °C min^{-1}. Black (x = 0), red (x = 0.5), green (x =1), blue (x = 1.5) and grey (x = 2.0).

Table 2. Oxygen content of $NdBaCo_{2-x}Mn_xO_{5+\delta}$ from TGA in air. The δ value at *RT* for the as-prepared samples ($\delta_{RT\ \text{as-prep}}$) is obtained from iodometric titration.

Manganese content (x)	$\delta_{RT\ \text{as-prep}}$	$\delta_{800\ °C\ \text{after 6 h isotherm}}$	$\delta_{RT\ \text{after cooling}}$
0	0.55	0.37	0.64
0.5	0.56	0.62	0.85
1.0	0.67	0.76	0.90
1.5	0.89	0.74	0.77
2.0	0.97	0.96	0.96

3. Structural and thermal behavior investigated by in situ XRD on heating in air

All of the as-prepared samples have been studied by high-temperature *in-situ* XRD in order to investigate the structural behavior as a function of temperature and determine the TEC. Figure 5 and Figure 6 show the XRD data collected for $x = 0$ and $x = 0.5$ compositions on heating in static air between100 and 300 °C. The $x = 0$ sample undergoes a phase transition from an orthorhombic (*Pmmm*) to a tetragonal (*P*4/*mmm*) structure marked by the evolution of the doublet (020, 200) peak to a single peak at $T \sim 200$ °C. The high temperature tetragonal phase is observed up to 800 °C in agreement with the literature [21, 46]. Similar structural phase transitions have been reported for the *Ln* = Pr [53] and Nd [21] samples at $T \sim 500$ and 400 °C, respectively. Streule *et al.* suggested them to be due to a thermally activated an oxygen vacancy order-disorder transition accompanying a Metal-Insulator transition [53]. The increase in the lattice parameters at $T > 350$ °C is due to oxygen loss (Figure 4) on reduction of the Co ions from Co^{4+} to Co^{3+}. In the temperature range 200 - 250 °C, the XRD patterns of the $x = 0.5$ sample consist of two tetragonal phases (Figure 6) with different δ values due to oxygen uptake, in agreement with TGA (Figure 4). At T ~250 °C, the two phases merge into a single tetragonal one whose *a*- and *c*-lattice parameters are respectively smaller and larger than those of the argon annealed as-prepared material.

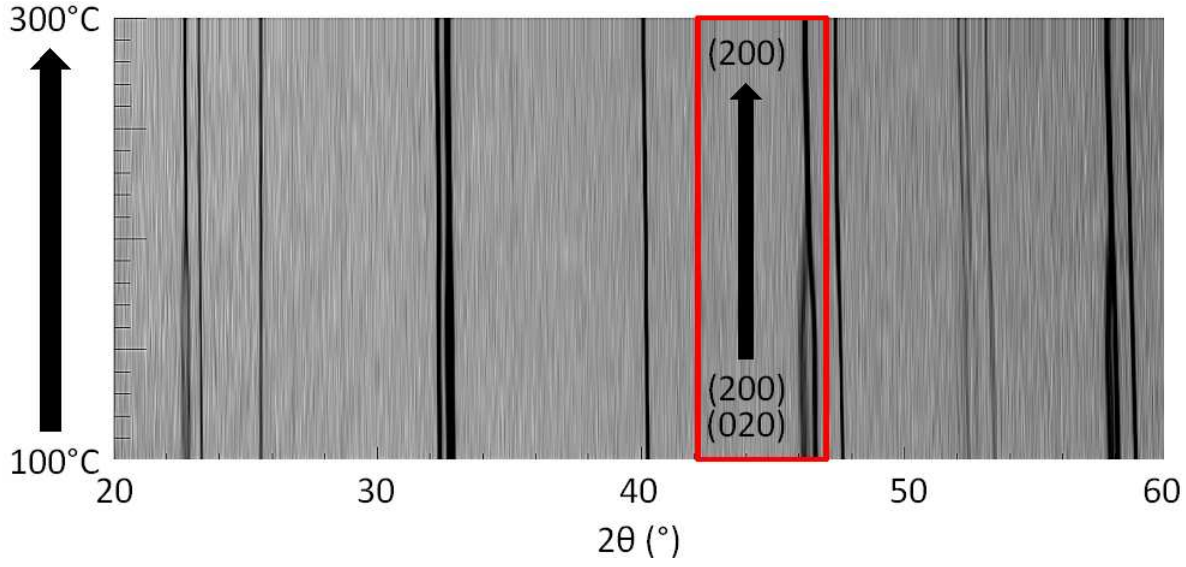

Figure 5. 2D surface plot of 1h-XRD patterns for $NdBaCo_2O_{5+\delta}$ collected in air at 20 °C intervals. The red rectangle highlights the phase transition from orthorhombic (S.G. *Pmmm*) to tetragonal symmetry (S.G. *P*4/*mmm*).

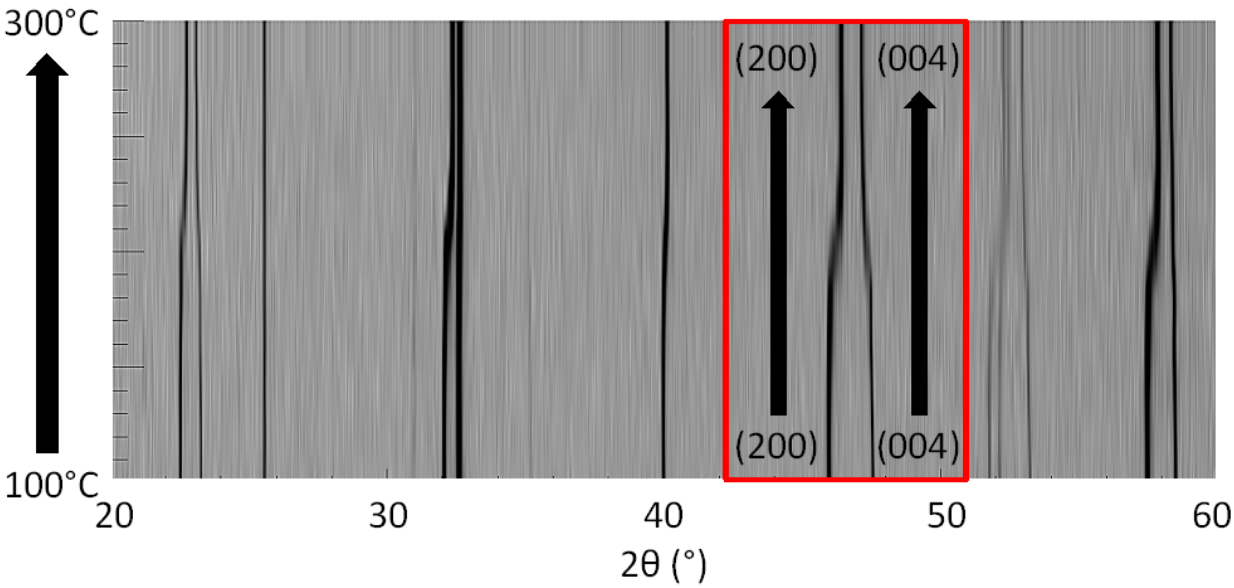

Figure 6. 2D surface plot of 1h-XRD patterns for $NdBaCo_{1.5}Mn_{0.5}O_{5+\delta}$ (x = 0.5) collected in air at 20 °C intervals. The red rectangle highlights *a*- and *c*-lattice contraction and expansion respectively, consecutive to oxygen uptake.

Besides thermal expansion, no major changes were detected in the XRD data collected on heating the x = 1.5 and 2.0 samples up to 300 °C, in agreement with insignificant oxygen uptake (Figure 4).

Because of the structural transition for x = 0 at T ~ 300 °C and the coexistence of two phases for the x = 0.5 and 1.0 samples up to ~ 250 °C, the average linear TEC for each material was estimated in the temperature range 300 - 800 °C, as:

$$\mathrm{TEC} = \frac{2 \times \alpha_a + \alpha_c}{3}$$

Where α_a and α_c are the linear thermal expansions along the *a*- and *c*- axes, respectively.

The results are plotted in Figure 7 and the average values are presented in Table 3. Although a linear variation is observed, it should be noted that the oxygen content is not constant in the temperature range 300-800 °C (Figure 4) and thermal expansion should consist of two constituents; one associated with atomic vibrations and the other related to change in the chemical composition.

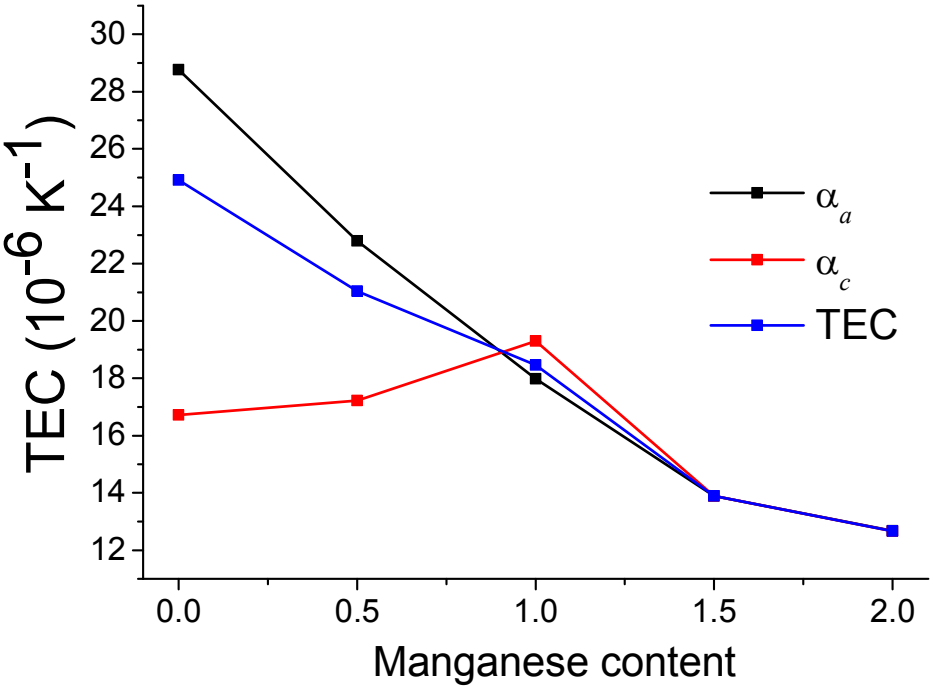

Figure 7. Linear thermal expansion coefficients for $NdBaCo_{2-x}Mn_xO_{5+\delta}$ from *in situ* XRD data on heating in air in the temperature range 300 - 800 °C; α_a and α_c are along the *a*- and *c-axes*, respectively and TEC corresponds to 1/3 ($2 \times \alpha_a + \alpha_c$).

Table 3. Average linear TEC values of $NdBaCo_{2-x}Mn_xO_{5+\delta}$ from high temperature *in situ* XRD.

Manganese content (*x*)	TEC (10^{-6} K^{-1})
0	24.8
0.5	21.0
1.0	18.4
1.5	13.9
2.0	12.6

The average TEC values of the $NdBaCo_{2-x}Mn_xO_{5+\delta}$ decrease with increasing Mn content from 24.8×10^{-6} K^{-1} for the $x = 0$ composition to 12.6×10^{-6} K^{-1} for the $x = 2.0$ one. The TECs of the $x = 0.5$ and 1.0 materials (Table 3) are still higher than those of common electrolyte materials such as $Ce_{0.8}Gd_{0.2}O_{1.9}$

(GDC) and $La_{0.8}Sr_{0.2}Ga_{0.83}Mg_{0.17}O_{2.815}$ (LSGM) which are 12.4 × 10^{-6} K^{-1} and 12 × 10^{-6} K^{-1}, respectively [54]. Considering the larger ionic radius of the high spin Co^{3+} (r = 0.61 Å) compared to that of the low spin ion (0.54 Å) [23], the spin state transition leads to a larger TEC for the Co-rich perovskites. The lower TEC in $NdBaCo_{2-x}Mn_xO_{5+\delta}$ with Mn substitution results from the lower fraction of Co^{3+} reducing the effect of the spin state transition. The average TEC values for the disordered perovskites x = 1.5 and 2.0 are 13.9 × 10^{-6} K^{-1} and 12.6 × 10^{-6} K^{-1}, respectively, which are close to those of GDC and LSGM. Assuming good chemical compatibility between the x = 1.5 and 2.0 electrode materials and LSGM or GDC electrolytes in SOFC operating conditions ($T \leq$ 800 °C), manganese substitution had the important advantage of improving mechanical compatibility.

4. Electrical conductivity measurements in air

Four point dc measurements have been performed in air on all the $NdBaCo_{2-x}Mn_xO_{5+\delta}$ materials. The samples annealed at 1200 °C have been heated at 800 °C for 12 h to equilibrate the oxygen concentration before starting the electrical conductivity measurements on cooling at 100 °C intervals.

The temperature dependence of electrical conductivity is plotted in Figure 8. The conductivity of the x = 0 and 0.5 samples increases with increasing temperature from 100 - 400 °C indicating a p-type thermally activated semiconducting behavior due to the hopping of small polarons. However, after a maximum is reached at 400 °C, the conductivity decreases with typical metallic behaviour because of significant loss of lattice oxygen [55] in agreement with the TGA data (Figure 4). The formation of oxide-ion vacancies accompanied by a reduction of Co^{4+} to Co^{3+} causes a decrease in the charge carrier concentration and covalent interaction because of a perturbation of the O-(Co,Mn)-O periodic potential and introduces carrier localization [56]. The conductivity of the x = 1.0, 1.5 and 2.0 samples exhibits semiconducting behavior in the whole temperature range. At a given temperature, the conductivity decreases with increasing Mn-content due to the decrease in the covalency of the (Co,Mn)-O bond. However, the conductivity value of the x = 2.0 sample is between that of the x = 0.5 and x = 1.0 compositions likely due to the Ba-deficiency at the *A*-site. At 700 °C, the conductivity values of the Mn-

containing samples are between 75 and 175 S cm^{-1} and at 800 °C, the values are larger than 100 S cm^{-1} which is sufficient for considering these materials as the air electrode for electrochemical cells.

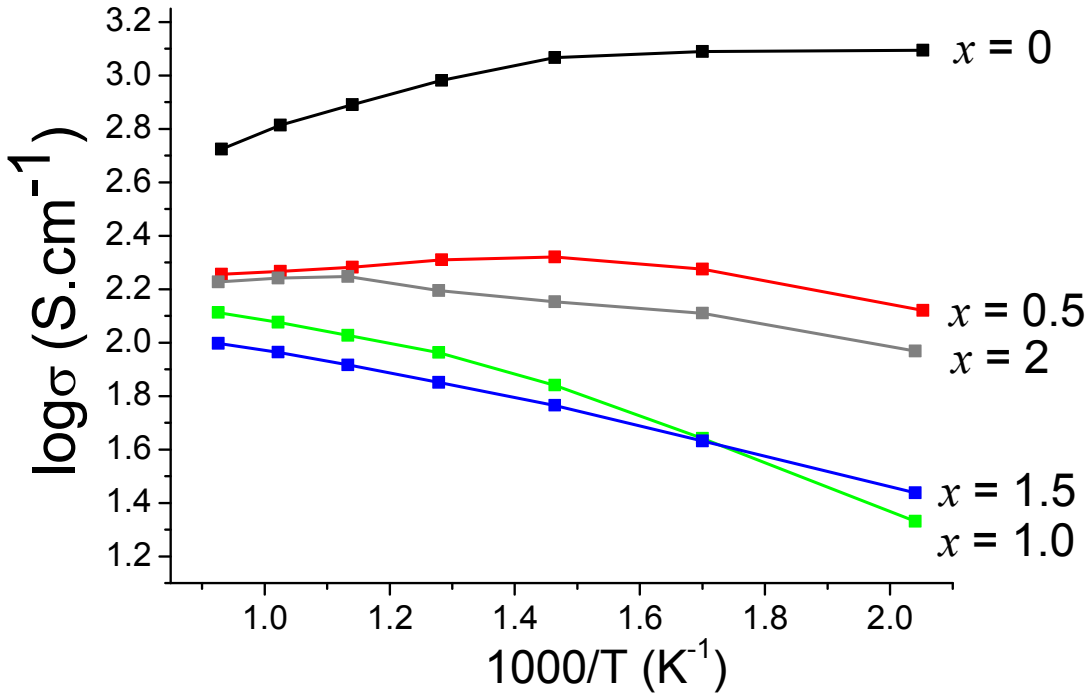

Figure 8. Arrhenius plot of the electrical conductivity of $NdBaCo_{2-x}Mn_xO_{5+\delta}$ collected in air on cooling.

The XRD patterns of the samples on which the electrical measurements have been performed show that the in-plane unit cell parameters have decreased after the heating/cooling cycle in air (Figure 9 a). The variation of the *c* lattice parameter is less straightforward. For the x = 0, 0.5 and 1 samples whose δ value increased after the heating/cooling cycle in air (Figure 4 and Table 2) the *c* lattice expands whereas for the x = 1.5 sample whose oxygen content decreased after the heating/cooling cycle in air, (Figure 4 and Table 2) the *c* parameter decreased (Figure 9 a) and the structure is no longer cubic. When the oxygen vacancies in the *Ln*O layer are filled, the octahedral distortion decreases and the *c*/*a* ratio approaches unity (Figure 9 b).

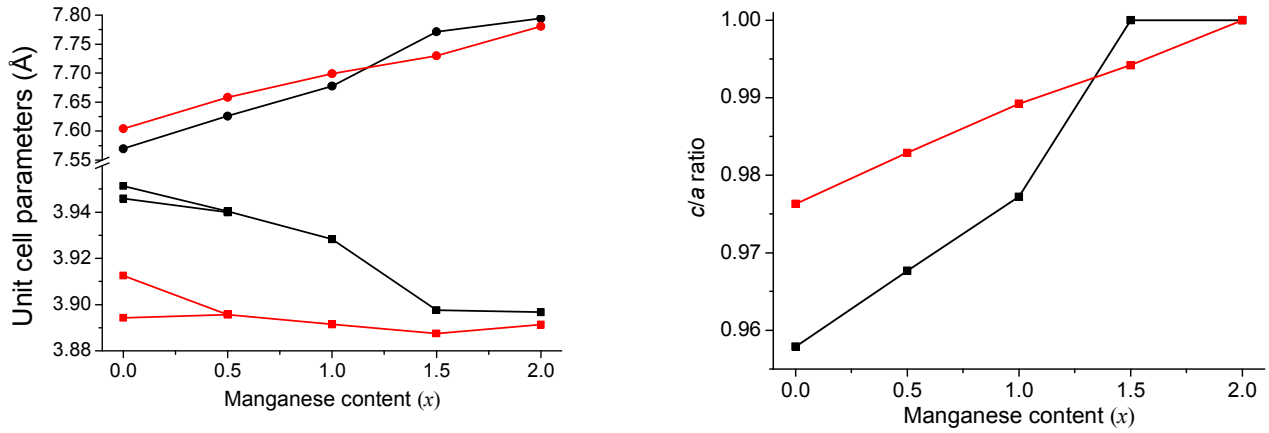

a) b)

Figure 9. (a) Unit cell lattice parameters of $NdBaCo_{2-x}Mn_xO_{5+\delta}$ at *RT*; (black) as-prepared and (red) after DC measurements. The *c* parameter of the disordered phases (*x* = 1.5 and 2.0) is multiplied by two for comparison with that of the layered perovskites (*x* = 0, 0.5 and 1.0); (b) Comparison of the perovskite distortion defined by the *c*/*a* ratio at *RT* between (black) as-prepared and (red) oxidized samples after a heating/cooling cycle in air up to 800 °C. The *c* lattice parameters of the *A*-site ordered samples (*x* = 0, 0.5 and 1.0) have been divided by two for comparison with that of the disordered samples (*x* = 1.5 and 2.0).

5. Reactivity of $NdBaCo_{2-x}Mn_xO_{5+\delta}$ with the GDC and LSGM electrolytes

Materials proposed for use as air cathodes in SOFCs have to be chemically inert to the electrolyte to ensure good connection. The elevated temperatures required to sinter the electrode material ($NdBaCo_{2-x}Mn_xO_{5+\delta}$) onto the SOFC electrolyte might cause formation of secondary phases at the electrode/electrolyte interface. If insulating interfacial phases are generated due to the interdiffusion of elements, they could increase the polarization resistance of the system. In order to check possible chemical interactions, the $NdBaCo_{2-x}Mn_xO_{5+\delta}$ cathode materials were mixed with the $La_{0.8}Sr_{0.2}Ga_{0.8}Mg_{0.2}O_{3-\delta}$ (LSGM) or $Ce_{0.8}Gd_{0.2}O_{1.95}$ (GDC) electrolyte in 50:50 mol % and fired during 36 h at 800 °C in air. Figure 10 shows the XRD patterns after this treatment. It was clear that the diffraction peaks of only $NdBaCo_{2-x}Mn_xO_{5+\delta}$ and LSGM or GDC were present with any new phases due to side reactions. The patterns of the mixtures have been analysed with the profile matching method (Le Bail). Comparison of the cell parameters of LSGM and GDC before and after the heat treatment show negligible variations (< 0.1% for LSGM and < 0.3% for GDC) consistent with negligible peak shift thus

suggesting that no apparent side reactions occur at $T \sim 800$ °C between the $NdBaCo_{2-x}Mn_xO_{5+\delta}$ cathode and the LSGM or GDC electrolyte materials. However, although XRD does not indicate the formation of new phases after firing at 800 °C, diffusion of ionic species across the interface between different phases could not be completely ruled out in SOFC manufacturing/fabrication conditions ($T \sim 1000$ °C).

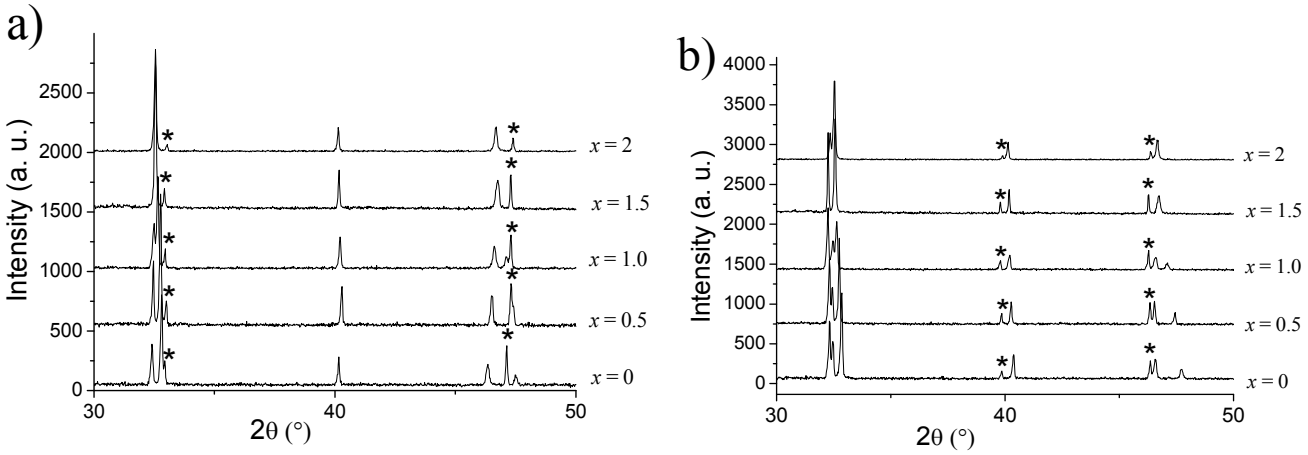

Figure 10. XRD data at *RT* of 50:50 mol % $NdBaCo_{2-x}Mn_xO_{5+\delta}$ and (a) GDC and (b) LSGM (b) mixtures after heating in air at 800 °C for 36 h. The peaks from the electrolyte are marked with (*).

Conclusion

The $NdBaCo_{2-x}Mn_xO_{5+\delta}$ ($0 \leq x \leq 2$) oxides have been synthesized by the EDTA-citrate complexing method. In structural terms, the as-prepared materials with $x \leq 1$ crystallize with an orthorhombic *Pmmm* or tetragonal *P*4/*mmm* symmetry whereas the manganese rich compositions with $x > 1$ do not exhibit *A*-site ordering and crystallize in the *Pm*-3*m* cubic symmetry. The electrical conductivity of the $NdBaCo_{2-x}Mn_xO_{5+\delta}$ materials in air decreases with increasing Mn content but all the samples show conductivity values > 100 S cm^{-1} at $T \sim 800$ °C. Chemical compatibility with the GDC and LSGM electrolytes reveals no side reactions up to 800 °C. While the conductivity is adequate to use them as electrode materials in SOFCs, the $NdBaCo_{2-x}Mn_xO_{5+\delta}$ ($x > 0$) offer an important advantage of excellent structural stability with no crystallographic phase transformation up to 800 °C unlike most of the Co-containing $ABO_{3-\delta}$ perovskites and significantly reduced TEC compared to $NdBaCo_2O_{5+\delta}$ suggesting

good long-term stability.

Acknowledgements

This work was supported partly by the ANR IDEA-MAT grant (ANR-A2-BS08-0012-01). We thank ANR for funding J. M. Hanlon.

References

1. S. J. Skinner, *International Journal of Inorganic Materials*, 2001, 3, 113-121.
2. R. A. De Souza and J. A. Kilner, *Solid State Ionics*, 1998, 106, 175-187.
3. D. J. L. Brett, A. Atkinson, N. P. Brandon and S. J. Skinner, *Chemical Society Reviews*, 2008, 37, 1568-1578.
4. J. A. Kilner, *Solid State Ionics*, 2000, 129, 13-23.
5. S. C. Singhal and K. Kendall, *High Temperature Solid Oxide Fuel Cells: Fundamentals, Design and Applications*, Oxford, 2003.
6. H. Ullmann, N. Trofimenko, F. Tietz, D. Stöver and A. Ahmad-Khanlou, *Solid State Ionics*, 2000, 138, 79-90.
7. S. Stephen J, *International Journal of Inorganic Materials*, 2001, 3, 113-121.
8. C. Frontera, A. Caneiro, A. E. Carrillo, J. Oró-Solé and J. L. García-Muñoz, *Chemistry of Materials*, 2005, 17, 5439-5445.
9. A. Tarancon, M. Burriel, J. Santiso, S. J. Skinner and J. A. Kilner, *Journal of Materials Chemistry*, 2010, 20, 3799-3813.
10. J. H. Kim, F. Prado and A. Manthiram, *Jouranl of the Electrochemical Society*, 2008, 155.
11. G. Kim, S. Wang, A. J. Jacobson, L. Reimus, P. Brodersen and C. A. Mims, *Journal of Materials Chemistry*, 2007, 17, 2500-2505.
12. A. Tarancon, S. J. Skinner, R. J. Chater, F. Hernandez-Ramirez and J. A. Kilner, *Journal of Materials Chemistry*, 2007, 17, 3175-3181.
13. J. H. Kim and A. Manthiram, *Journal of the Electrochemical Society*, 2008, 155, 385-390.
14. L. Er-Rakho, C. Michel, P. Lacorre and B. Raveau, *Journal of Solid State Chemistry*, 1988, 73, 531-535.
15. V. Caignaert, I. Mirebeau, F. Bourée, N. Nguyen, A. Ducouret, J. M. Greneche and B. Raveau, *Journal of Solid State Chemistry*, 1995, 114, 24-35.
16. Y. Moritomo, M. Takeo, X. J. Liu, T. Akimoto and A. Nakamura, *Physical Review B*, 1998, 58, R13334-R13337.
17. I. O. Troyanchuk, N. V. Kasper, D. D. Khalyavin, H. Szymczak, R. Szymczak and M. Baran, *Physical Review B*, 1998, 58, 2418-2421.
18. A. Maignan, C. Martin, D. Pelloquin, N. Nguyen and B. Raveau, *Journal of Solid State Chemistry*, 1999, 142, 247-260.
19. V. Pralong, V. Caignaert, S. Hebert, A. Maignan and B. Raveau, *Solid State Ionics*, 2006, 177, 1879-1881.
20. J. C. Burley, J. F. Mitchell, S. Short, D. Miller and Y. Tang, *Journal of Solid State Chemistry*, 2003, 170, 339-350.

21. J. H. Kim, L. Mogni, F. Prado, A. Caneiro, J. A. Alonso and A. Manthiram, *Journal of the Electrochemical Society*, 2009, 156, B1376-B1382.
22. M. A. Señarís-Rodríguez and J. B. Goodenough, *Journal of Solid State Chemistry*, 1995, 118, 323-336.
23. K. Huang, H. Y. Lee and J. B. Goodenough, *Journal of The Electrochemical Society*, 1998, 145, 3220-3227.
24. M. A. Señarís-Rodríguez and J. B. Goodenough, *Journal of Solid State Chemistry*, 1995, 118, 323-336.
25. J. H. Kim and A. Manthiram, *Electrochimica Acta*, 2009, 54, 7551-7557.
26. S. Choi, J. Shin and G. Kim, *Journal of Power Sources*, 2012, 201, 10-17.
27. H. Ding and X. Xue, *Journal of Power Sources*, 2010, 195, 4718-4721.
28. Y. N. Kim and A. Manthiram, *Journal of The Electrochemical Society*, 2011, 158, B276-B282.
29. T. V. Aksenova, A. S. Urusova, L. Y. Gavrilova and V. A. Cherepanov, *Journal of Alloys and Compounds*, 2014, 590, 474-478.
30. Y. N. Kim, J. H. Kim and A. Manthiram, *Journal of Power Sources*, 2010, 195, 6411-6419.
31. V. A. Cherepanov, T. V. Aksenova, L. Y. Gavrilova and K. N. Mikhaleva, *Solid State Ionics*, 2011, 188, 53-57.
32. F. Jin, H. Xu, W. Long, Y. Shen and T. He, *Journal of Power Sources*, 2013, 243, 10-18.
33. I. Troyanchuk, S. Trukhanov and G. Szymczak, *Crystallography Reports*, 2002, 47, 658-665.
34. S. Trukhanov, V. Khomchenko, L. Lobanovski, M. Bushinsky, D. Karpinsky, V. Fedotova, I. Troyanchuk, A. Trukhanov, S. Stepin, R. Szymczak, C. Botez and A. Adair, *J. Exp. Theor. Phys.*, 2006, 103, 398-410.
35. S. Trukhanov, A. Trukhanov, H. Szymczak, C. Botez and A. Adair, *Journal of Low Temperature Physics*, 2007, 149, 185-199.
36. S. V. Trukhanov, I. O. Troyanchuk, M. Hervieu, H. Szymczak and K. Barner, *Physical Review B*, 2002, 66.
37. A. Snedden, A. J. Wright and C. Greaves, *Materials Research Bulletin*, 2008, 43, 2403-2412.
38. V. Pralong, V. Caignaert, S. Hebert, A. Maignan and B. Raveau, *Solid State Ionics*, 2006, 177, 1879-1881.
39. F. Millange, V. Caignaert, B. Domenges, B. Raveau and E. Suard, *Chemistry of Materials*, 1998, 10, 1974-1983.
40. I. D. Seymour, A. Chroneos, J. A. Kilner and R. W. Grimes, *Physical Chemistry Chemical Physics*, 2011, 13, 15305-15310.
41. K. Zhang, L. Ge, R. Ran, Z. Shao and S. Liu, *Acta Materialia*, 2008, 56, 4876-4889.
42. J. Rodríguez-Carvajal, *Physica B: Condensed Matter*, 1993, 192, 55-69.
43. G. H. Jonker and J. H. Van Santen, *Physica*, 1950, 16, 337-349.
44. T. Negas and R. S. Roth, *Journal of Solid State Chemistry*, 1971, 3, 323-339.
45. T. V. Aksenova, L. Y. Gavrilova, A. A. Yaremchenko, V. A. Cherepanov and V. V. Kharton, *Materials Research Bulletin*, 2010, 45, 1288-1292.
46. Y. Hu, O. Hernandez, T. Broux, M. Bahout, J. Hermet, A. Ottochian, C. Ritter, G. Geneste and G. Dezanneau, *Journal of Materials Chemistry*, 2012, 22, 18744-18747.
47. P. S. Anderson, C. A. Kirk, J. Knudsen, I. M. Reaney and A. R. West, *Solid State Sciences*, 2005, 7, 1149-1156.
48. J. P. Chapman, J. P. Attfield, M. Molgg, C. M. Friend and T. P. Beales, *Angewandte Chemie International Edition in English*, 1996, 35, 2482-2484.
49. D. Akahoshi, M. Uchida, Y. Tomioka, T. Arima, Y. Matsui and Y. Tokura, *Physical Review Letters*, 2003, 90, 177203.
50. S. Pang, X. Jiang, X. Li, Q. Wang and Z. Su, *Journal of power sources*, 2012, 204, 53-59.
51. J. E. Huheey, E. A. Keiter and R. L. Keiter, *Inorganic chemistry : principles of structure and reactivity*, HarperCollins, [S.l.], 1993.
52. R. D. Shannon, *Acta Crystallographica Section A*, 1976, 32, 751-767.

53. S. Streule, A. Podlesnyak, E. Pomjakushina, K. Conder, D. Sheptyakov, M. Medarde and J. Mesot, *Physica B: Condensed Matter*, 2006, 378-380, 539-540.
54. V. V. Kharton, F. M. B. Marques and A. Atkinson, *Solid State Ionics*, 2004, 174, 135-149.
55. C. Frontera, J. L. Garcia-Muñoz, A. Llobet, L. Mañosa and M. A. G. Aranda, *Journal of Solid State Chemistry*, 2003, 171, 349-352.
56. H. Takahashi, F. Munakata and M. Yamanaka, *Physical Review B*, 1998, 57, 15211-15218.

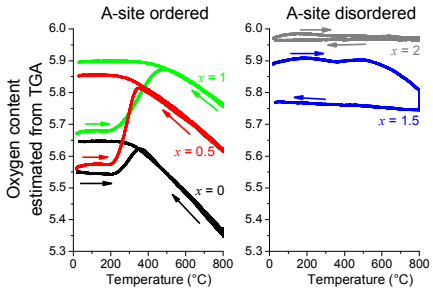

TGA for $NdBaCo_{2-x}Mn_xO_{5+\delta}$ in air with heating/cooling at 2 °C min^{-1} and an intermediate step at 800°C for 6h.